

# CHANG-ES VIII: Uncovering Hidden AGN Activity in Radio Polarization

Judith A. Irwin<sup>1</sup>, Philip Schmidt<sup>2</sup>, A. Damas-Segovia<sup>2</sup>, Rainer Beck<sup>2</sup>, Jayanne English<sup>3</sup>  
George Heald<sup>4</sup> Richard N. Henriksen<sup>1</sup>, Marita Krause<sup>2</sup>, Jiang-Tao Li<sup>5</sup>, Richard J. Rand<sup>6</sup>, Q.  
Daniel Wang<sup>7</sup>, Theresa Wiegert<sup>1</sup>, Patrick Kamieneski<sup>7</sup>, Dylan Paré<sup>7</sup>, and Kendall Sullivan<sup>7</sup>

## ABSTRACT

We report on C-band (5 - 7 GHz) observations of the galaxy, NGC 2992, from the CHANG-ES sample. This galaxy displays an embedded nuclear double-lobed radio morphology within its spiral disk, as revealed in linearly polarized emission but *not* in total intensity emission. The radio lobes are kpc-sized, similar to what has been observed in the past for other Seyfert galaxies, and show ordered magnetic fields. NGC 2992 has shown previous evidence for AGN-related activity, but not the linearly polarized radio features that we present here. We draw attention to this galaxy as the first clear example (and prototype) of bipolar radio outflow that is revealed in linearly polarized emission only. Such polarization observations, which are unobscured by dust, provide a new tool for uncovering hidden weak AGN activity which may otherwise be masked by brighter unpolarized emission within which it is embedded. The radio lobes observed in NGC 2992 are interacting with the surrounding interstellar medium and offer new opportunities to investigate the interactions between nuclear outflows and the ISM in nearby galaxies. We also compare the radio emission with a new CHANDRA X-ray image of this galaxy. A new CHANG-ES image of NGC 3079 is also briefly shown as another example as to how much more obvious radio lobes appear in linear polarization as opposed to total intensity.

*Subject headings:* galaxies: individual (NGC 2992) — galaxies: active — galaxies: jets — galaxies: nuclei

<sup>1</sup>Dept. of Physics, Engineering Physics, & Astronomy, Queen's University, Kingston, Ontario, Canada, K7L 3N6  
irwin@astro.queensu.ca, henriksn@astro.queensu.ca, twiegert@astro.queensu.ca .

<sup>2</sup>Max-Planck-Institut für Radioastronomie, Auf dem Hügel 69, 53121, Bonn, Germany,  
pschmidt@mpifr-bonn.mpg.de, adamas@mpifr-bonn.mpg.de, rbeck@mpifr-bonn.mpg.de, mkrause@mpifr-bonn.mpg.de.

<sup>3</sup>Department of Physics and Astronomy, University of Manitoba, Winnipeg, Manitoba, Canada, R3T 2N2  
jayanne.english@umanitoba.ca.

<sup>4</sup>CSIRO Astronomy and Space Science, 26 Dick Perry Avenue, Kensington WA 6151, Australia; Netherlands Institute for Radio Astronomy (ASTRON), Postbus 2, 7990 AA, Dwingeloo, The Netherlands  
George.heald@csiro.au

<sup>5</sup>Department of Astronomy, University of Michigan, 409 West Hall, 1085 S. University, Ann Arbor, MI, 48109  
jiangtal@umich.edu.

<sup>6</sup>Dept. of Physics and Astronomy, University of New Mexico, 1919 Lomas Boulevard, NE, Albuquerque, NM,

## 1. Introduction

The powerful jet and double-lobed character of radio emission around distant massive elliptical galaxies is well known and originates in the active galactic nuclei (AGNs) of their host galaxies. Indeed, since it is believed that the formation of a supermassive black hole (SMBH) is closely connected to the formation of the bulge mass, with both evolving together (Ferrarese & Merritt 2000; Gebhardt et al. 2000; Zheng et al. 2009; Kormendy & Ho 2013), one would expect AGN-related activity to manifest itself in spirals as well. Yet, spiral galaxies do not generally show such

87131, USA rjr@phys.unm.edu.

<sup>7</sup>Dept. of Astronomy, University of Massachusetts, 710 North Pleasant St., Amherst, MA, 01003, USA,  
wqd@astro.umass.edu, pkamieneski@umass.edu, dpare@umass.edu, kendallsulli@umass.edu.

impressive evidence for nuclear activity and observations of AGNs in spirals are relatively rare. The incidence of radio AGN in late type galaxies, for instance, is about an order of magnitude lower than in early-type galaxies (Kaviraj et al. 2015b). Those spiral galaxies that do display nuclear outflows in the form of AGN-related jet and/or lobe-like features make for a short list. For example, Seyfert galaxies can harbour jets on pc to kpc scales (Ho & Ulvestad 2001, and references therein). Well-known examples also include NGC 3079 (Irwin & Seaquist 1988; Hummel, van Gorkom, & Kotanyi 1983), the Circinus spiral galaxy (Harnett et al. 1990; Greenhill et al. 2003), NGC 7479 (Laine & Beck 2008), NGC 4388 (Damas-Segovia et al. 2016), NGC 4258 (Greenhill et al. 1995; Miyoshi et al. 1995; Herrnstein et al. 1998; Krause & Löhner 2004), as well as the spectacular examples, 0313-192 (Ledlow et al. 2001; Keel et al. 2006), ‘Specs’ (Hota et al. 2011), J23450449 (Bagchi et al. 2014), and J1649+2635 (Mao et al. 2015).

The reason for the apparent relative scarcity of such activity in spirals is not entirely clear, though a variety of possibilities have been raised. For example, advection-dominated accretion flow may result in very little radiation (Narayan & Yi 1995; Yuan & Narayan 2014), the SMBHs in spirals may not be massive enough to produce the large-scale jets seen in ellipticals (Laor 2000), accreting SMBHs in spirals may not be spinning rapidly enough (Wilson & Colbert 1995; Sikora et al. 2007; Tchekhovskoy et al. 2010; Dotti et al. 2013) or the magnetic flux could be insufficient to launch jets (Sikora & Begelman 2013). Other issues such as the effect of the dense surrounding interstellar medium (ISM) on the outflow (Dasyra et al. 2015), the difficulty in accreting high angular momentum gas, the possibility of episodic outflows (Márquez et al. 2003), and environmental effects such as perturbations from nearby galaxies, all have yet to be fully understood and quantified.

An additional complicating issue is that nuclear outflows can also originate from a central starburst (Veilleux et al. 2005, and references therein) and both may be occurring in the same galaxy (e.g. NGC 3079 Shafi et al. 2015, and references therein). It has thus been difficult to identify the origin of an observed outflow as being due to star formation (SF), or an AGN, or some combination

thereof. An active low-luminosity AGN (LLAGN), for example, could be embedded in a nuclear region with abundant SF activity. Since all spirals host star formation, the issue is really whether or not an AGN is also present and how best to identify it.

Hard X-ray emission is an indicator of AGN activity, provided the luminosity exceeds what is expected from ultra-luminous X-ray sources ( $10^{39-42}$  ergs/s) (Mushotsky 2004). Optical emission line ratios that indicate the presence of a hard ionizing continuum is another (Baldwin, Phillips & Terevelich 1981) although dust obscuration can be problematic, especially for edge-on galaxies. The mid-IR PAH<sup>1</sup> to continuum ratio has been used as a SF/AGN diagnostic for distant galaxies (Kirkpatrick et al. 2015) and other mid-IR line ratios (see Pereira-Santaella et al. 2010) have also been shown to be effective.

Evidence for an AGN, however, is not necessarily evidence for AGN-related outflows. As indicated above, it is in the radio continuum that jets and lobes have historically been detected, since synchrotron emission is a strong component of such outflow. AGN-related outflows have been identified by the presence of linear structures in Seyfert galaxies (Ulvestad & Wilson 1984) or by small-scale jets in late-type spirals (Kaviraj et al. 2015a), but only in in *total intensity* radio continuum (Ulvestad & Wilson 1984). In order to be so identified, such emission must dominate any SF-related emission in the vicinity.

In this paper, we provide a new diagnostic for identifying AGN-related outflow via radio polarization, specifically *bipolar radio features or other evidence for AGN-related outflows that are masked in total intensity but are revealed in linear polarization*. In other words, LLAGNs may not, in fact, be rare, but require that our observations be targeted at the polarized rather than the total intensity radio emission to be clearly seen.

Polarization images are well-suited to uncovering previously hidden AGNs because of their sensitivity to ordered magnetic fields that are prevalent in the outflows and also because the radio emission is insensitive to dust obscuration. As part of the CHANG-ES program (‘Continuum Halos in Nearby Galaxies – an EVLA Survey’, Irwin et al.

<sup>1</sup>Polycyclic Aromatic Hydrocarbon

2012), we focus on one such galaxy at C-band (6 GHz), i.e. NGC 2992, which we take to be a prototype for such activity. This galaxy was previously known to harbour an active nucleus (Sect. 2) but now the polarized radio emission clearly shows the outflows.

Note that NGC 2992 is *not* the only AGN in the CHANG-ES sample. A more complete census of AGNs in the CHANG-ES sample will be presented in a future paper. For a list of radio polarization observations and magnetic fields that have been observed in other mostly non-edge-on nearby galaxies, see the appendices of Beck & Wielebinski (2013).

## 2. NGC 2992 and its AGN

NGC 2992 (Fig. 1,  $D = 34$  Mpc, Wiegert et al. 2015) is a well-known Seyfert galaxy (Osmer et al. 1974; Ward et al. 1980) that is interacting with its primary companion, NGC 2993,  $\sim 3$  arcmin to the SE as well as Arp 245N  $\sim 2$  arcmin to the NE (see also Fig. 6). Duc et al. (2000) have shown that an additional smaller galaxy, FGC 0938,  $\sim 5$  arcmin to the SW is also part of this system, collectively known as Arp 245. The result is that NGC 2992 is highly disturbed. For example, Duc et al. list the galaxy’s inclination at 70 degrees. However, in the central  $\sim 1$  arcmin where we detect continuum emission, optical isophotes<sup>2</sup> suggest an inclination of 64 degrees assuming a thin disk. Note that the near side of the galaxy is the west side (Veilleux et al. 2001).

A variety of evidence has already pointed to nuclear activity in this galaxy. A large scale radio feature extends  $\approx 30$  arcsec (5 kpc) to the SE (Hummel, van Gorkom, & Kotanyi 1983; Ward et al. 1980) which we also detect in total intensity (Fig. 1) and refer to as the ‘southeast extension’. Higher resolution radio continuum observations by Ulvestad & Wilson (1984) and Wehrle & Morris (1988) show emission within the central 10 arcsec of the galaxy in the form of a double loop that is limb-brightened and centered on the nucleus. Our data do not resolve the double-loop and instead this region appears as a central oval-shaped region at a position angle of 170 degrees in Fig. 1 (the ‘central oval’). Chapman et al. (2000) sug-

gest that multiple radio components are superimposed in this region. Hard mid-IR line ratios of 2.1 and 2.8 for  $[\text{NeII}](12.81 \mu\text{m})/[\text{NeV}](14.32 \mu\text{m})$  and  $[\text{OIV}](25.89 \mu\text{m})/[\text{NeII}](12.81 \mu\text{m})$ , respectively, place NGC 2992 firmly in the Seyfert/AGN part of the diagnostic plots of Pereira-Santaella et al. (2010) (their Figs. 5 and 6).

Evidence for nuclear radial outflows have also been found in optical emission lines (Colina et al. 1987; Tsvetanov, Dopita, & Allen 1995; Colbert et al. 1996; Marquez et al. 1998; Veilleux et al. 2001); detailed analyses of optical emission lines can be found in Allen et al. (1999) and Garcia-Lorenzo et al. (2001). Its Seyfert classification has changed with time between 1.5 and 2 within a few years (Trippe et al. 2008). The optical outflows have been attributed predominantly to the AGN rather than a nuclear starburst (Friedrich et al. 2010).

NGC 2992 has long been known to be an X-ray source and the X-ray emission varies (Maccacaro, Perola, & Elvis 1982; Elvis et al. 1990; Kruper, Urry, & Canizares 1990; Weaver et al. 1996; Gilli et al. 2000; Beckmann et al. 2007; Shu et al. 2010) (flares) on timescales of days to weeks (Shu et al. 2010). The companion galaxy, NGC 2993, is also an X-ray source (Colbert et al. 1998). An infrared outburst was detected in 1988 (Glass 1997). Colbert et al. (2005) conclude that the extranuclear soft X-ray luminosity could be explained either by a star-burst-driven or AGN-driven wind.

In summary, there is compelling prior evidence for an AGN in NGC 2992. In total intensity radio emission, however, only the eastern extension and inner double-loop (within our central oval) have previously indicated that AGN-related outflow has occurred.

## 3. Observations and Data Reductions

### 3.1. Individual Configurations

Our CHANG-ES data include both C-band (6 GHz) and L-band (1.6 GHz) observations using the Karl G. Jansky Very Large Array (hereafter the VLA) in a variety of array configurations. Here, we report on the C-band observations only, since no linear polarization is observed at L-band with a fractional polarization (P/I) that is above 0.5% in either array configuration; this is likely due to Faraday depolarization at the lower fre-

<sup>2</sup>Measured from the DSS2 blue image since an SDSS image is not available.

quency. The C-band observations were obtained in the C and D configurations of the VLA. The largest spatial scale detectable by the VLA at C-band is 4 arcmin; since the entire field of view shown in Fig. 1 is only 1.6 arcmin, we should not have missed any significant short-spacing flux. A summary of the observations and image parameters is given in Table 1.

Data reduction and imaging details are described in Irwin et al. (2013) and Wiegert et al. (2015). Here we provide a brief outline. The Common Astronomy Software Applications (CASA) package (McMullin et al. 2007) was used throughout<sup>3</sup>.

Each galaxy was observed within a scheduling block that included other galaxies so that the uv coverage could be maximized for each. The calibrators were 3C 286 which was used for the primary gain and phase calibration as well as the bandpass and polarization angle calibration, J1407+2827 (OQ208) which was used to calibrate the polarization leakage, and finally the secondary gain and phase calibrators, J0837-1951 and J0943-0819 for NGC 2992 in D and C configurations, respectively.

The frequency coverage was from 4.979 → 7.021 (2.042 GHz) and observations were carried out in spectral line mode with 16 spectral windows across the band (each 128 MHz wide). Each spectral window contained 64 spectral channels for a total of 1024 channels across the entire band.

Flagging was carried out manually and any flagging that applied to the total intensity data (RR and LL circular polarizations) was automatically applied to the cross-polarizations (RL and LR). Additional flagging was then carried out for RL and LR as required.

Wide-field imaging (Cornwell, Golap & Bhatnagar 2008) was carried out using the multi-scale multi-frequency synthesis (ms-mfs) algorithm (Cornwell 2008; Rau & Cornwell 2011), with simultaneous fitting of a simple power law ( $S_\nu \propto \nu^\alpha$ ) across the band. For all maps from the individual observing runs, Briggs robust = 0 uv weighting was used (Briggs 1995) as implemented in CASA<sup>4</sup>. Self-calibration iterations

<sup>3</sup><http://casa.nrao.edu>

<sup>4</sup>A second set of maps using a uv taper was also made for internal comparison but are not presented here.

were also carried out for the total intensity image (Table 1) until no further improvement in the dynamic range resulted.

Imperfect phase and amplitude calibrations produce errors that normally be below the rms for

The dynamic range of the total intensity images are very high (e.g.  $\approx 8000/1$  at C-configuration) and therefore imperfect phase and amplitude calibrations result in some residual sidelobes that could not be cleaned out completely. Hence we show our first contours at levels that are higher than is normally shown (Fig. 1).

For each observation, Stokes Q and U were imaged using the same self-calibration table and the same input parameters as for total intensity. Maps of linear polarization,  $P = \sqrt{Q^2 + U^2 - \sigma_{Q,U}^2}$  were then made, where  $\sigma_{Q,U}$  is the rms noise of the Q and U maps. The latter term does a zeroth order correction for the fact that P images are positively biased (e.g. Simmons & Stewart 1985; Vailancourt 2006; Everett & Weisberg 2001) and is the only correction that is currently implemented in CASA. In this correction some very low level emission becomes negative and those negatives are then blanked. Polarization angle maps were then also made with a  $3\sigma_{Q,U}$  cut off.

All maps were then corrected for the primary beam (PB, full-width at half-maximum = 7.5 arcmin). We show our resulting images without the PB correction (unless otherwise indicated – see next section) so that the noise is uniform; however, any measurements are made on the PB-corrected images, and so throughout. Note that the source is only about 1 arcmin in size so that PB corrections are minor<sup>5</sup>.

### 3.2. Combined Configurations and Rotation Measure (RM) Synthesis

We combined the C and D configuration uv data into a single large data set in order to obtain the highest possible signal-to-noise (S/N) ratio with sensitivity to a wide range of spatial scales. In addition, we carried out an RM Synthesis anal-

<sup>5</sup>Recent PB measurements are now available for the VLA (EVLA Memo 195, R. Perley) though (at the time of writing) have not yet been implemented into CASA; the FWHM is about 6% smaller than previously thought at C-band.

ysis to correct for Faraday rotation, as follows.

Both the C and D configuration uv data were imaged simultaneously to make two new images of ‘low resolution’ and ‘high resolution’ which resulted from modifying the Briggs robustness parameter and uvtaper (Table 1). The total intensity images were made in the same way as described in Sect. 3.1 except for the different input parameters which are listed in the table<sup>6</sup>. The original images had marginally smaller beams than quoted in the table and were then smoothed to the resolutions indicated; this was to ensure that the total intensity and polarized intensity resolutions matched exactly since they are formed using different processes (see below). Attempts were made to do additional self-calibration of the combined configuration data sets; however such attempts did not improve the dynamic range of the images.

For the linear polarization imaging, we produced combined-configuration Q and U cubes with dimensions of RA, DEC, and frequency. For each image plane along the frequency axis, we averaged the data over each spectral window so that we sample the entire band with a new channel separation of 128 MHz. Images for each new channel were then smoothed to the resolution of the spectral window with the lowest resolution and then PB-corrected using the primary beam that corresponds to the center of its channel.

Stokes Q, U and polarized intensity (PI) cubes in dimensions, RA, DEC, Faraday depth,  $\phi$ , were then generated using the RM synthesis code of Brentjens & de Bruyn (2005). The Faraday depth of a source is defined as

$$\phi(\vec{r}) = 0.81 \int_{\vec{r}}^0 n_e \vec{B} \cdot d\vec{r} \text{ rad m}^{-2} \quad (1)$$

where  $B$  is the magnetic field strength in  $\mu\text{G}$ ,  $n_e$  is the electron number density in  $\text{cm}^{-3}$ , and  $r$  is the line-of-sight path length in pc. The  $\phi$  axis of the cubes extends from -1000 to +1000  $\text{rad m}^{-2}$  so that  $\phi \delta\lambda^2 \ll 1$  is fulfilled (where we assumed  $\delta\lambda^2$  to be the difference in wavelength squared that corresponds to the separation between the two lowest frequency channels) and hence no sig-

nificant Faraday depolarization between adjacent frequency channels occurs.

The following data products were then extracted from the Faraday cubes via an algorithm kindly supplied by B. Adebahr (private communication): a) a PI map, consisting of the maximum value along the  $\phi$  axis of the PI cube for each pixel, b) a map of the  $\phi$  value at which the maximum PI occurs, c) a map of apparent polarization position angles corresponding to the  $\phi$  value at which the maximum PI occurs, and d) a map of de-rotated (corrected) polarization position angle which also corresponds to the location at which PI is maximum. Maps that show  $\phi$  at the highest polarized flux density in the Faraday depth spectra, and of the intrinsic polarization angle for this  $\phi$ , were computed only in regions where the polarized intensity is higher than  $4\sigma$  in the Faraday Q and U image planes.

The width of the  $\lambda^2$  distribution probed in C-band leads to a RM spread function with a main peak FWHM of  $2000 \text{ rad m}^{-2}$ , which implies that potentially present emission at multiple Faraday depths is not resolved. We therefore assume for our further analysis that emission on any given line of sight appears at a single Faraday depth. While it would hence be possible to measure Faraday depths at a similar accuracy by computing ‘classical’ RMs between different sections of the frequency band (the  $n\pi$  ambiguity is not a major issue at C-band), our main purpose of applying RM synthesis instead is to improve our sensitivity to the polarized emission. Moreover, due to the poor resolution in Faraday depth, a deconvolution of the Faraday spectra was not necessary.

Since maps made as a result of RM synthesis must necessarily be corrected for the PB at a prior stage, any combined-configuration polarization images are shown with PB correction. Rms noise values are then a function of position on the map and we quote averages in Table 1 in these cases.

## 4. Results

In this section we first present the results for the individual configurations (C and D) separately, and then the results for combined (C+D) configurations, RM corrected. We consider each step

<sup>6</sup>The *multiscales* parameters were also slightly different from the individual configurations, but they matched between the total intensity and corresponding polarized intensity images.

TABLE 1  
C-BAND OBSERVATIONS AND IMAGING OF NGC 2992

Observation	Date <sup>a</sup>	$\nu_0^b$ (GHz)	uv Weighting <sup>c</sup>	Beam parameters <sup>d</sup> ", ", deg.	Pixel size "	SC Iterations <sup>e</sup>	rms noise <sup>f</sup> I Q,U ( $\mu\text{Jy beam}^{-1}$ )
<b>Individual</b>							
D configuration	13-Dec-2011	6.000	Rob=0	14.33, 8.84, -13.3	1.0	2A&P	8.4 8.0
C configuration	07-Apr-2012	6.000	Rob=0	4.12, 2.48, -8.0	0.5	4P+1A&P	3.5 3.2
<b>Combined</b>							
C+D configuration (low resolution)		6.000	Rob=+2 (22 klambda)	10.0,10.0,0.0	0.5		15.0 3.5
C+D configuration (high resolution)		6.000	Rob=-2	5.20, 3.10, -9.5	0.5		5.0 7.7

<sup>a</sup>Date that the observations were carried out (UTC).

<sup>b</sup>Central frequency of each image. The bandwidth, before flagging, was 2 GHz.

<sup>c</sup>Briggs ‘Robust’ weighting as implemented in CASA. Value in parentheses indicates the value of the uv taper for the low resolution combined configuration image.

<sup>d</sup>Major & minor axis diameters and position angle of the synthesized beam.

<sup>e</sup>Number of self-calibration iterations that were applied to improve the maps. Each iteration acted on the non-self-calibrated data, but using an improved model. P: phase-only, A&P: amplitude and phase.

<sup>f</sup>Rms noise for the total intensity (I) and Stokes Q and U maps. For Q and U of the combined configuration maps for which RM synthesis was carried out, these are averages of the PB-corrected maps over the full-width-half-maximum PB area.

since it is helpful to see how the configurations emphasize certain spatial scales in the source and also to see the extent to which improvements result from the combination of these configurations. In addition, we wish to see the extent to which Faraday-rotation may or may not alter the magnetic field vectors for this disturbed edge-on galaxy at C-band. Little has been published so far in the literature regarding wide-band polarization data and the improvements that can result from these two steps. We finally present new CHANDRA X-ray results for NGC 2992.

#### 4.1. Results – Individual Configurations

Fig. 1 shows a number of new features in NGC 2992 at both low and high resolution. The outer contours (D-configuration) reveal the SE extension mentioned above, as well as extensions to the north and south; the latter appear to be offset from the inner disk angle but do appear to align with some spiral arm structure. The inner contours (C-configuration) also show emission extending away from the central oval. The ‘west extension’ is particularly noteworthy (see below).

The total flux density at 6.0 GHz is  $80.4 \pm 1.6$  mJy (Wiegert et al. 2015) and the global spectral index between L-band (1.6 GHz) and C-band (6 GHz) is  $\alpha_{L-C} = -0.70 \pm 0.02$  (Li et al. 2016).

This is flatter than the majority of CHANG-ES galaxies for which  $\alpha_{L-C} \approx -0.9$ , except for outliers with known AGNs (Li et al. 2016, their Fig. 4a), i.e. NGC 2992 has a global spectral index that is suggestive of an AGN, in agreement with previous knowledge about this galaxy. The *in-band* spectral index (see Wiegert et al. 2015, for a full description) of the highest resolution ( $\sim 3.3$  arcsec = 540 pc) C-configuration data within the half-power-beam-width centered at the nucleus is  $\alpha_C(\text{nuc}) = -0.78 \pm 0.01$ . These values clearly indicate that non-thermal emission is dominant at C-band.

The linear polarization images (Fig. 2) are quite revealing. The D-configuration C-band image (top) shows apparent magnetic field (B) vectors<sup>7</sup> in coherent structures, pointing roughly away from the galaxy’s center. *These vectors have not yet been corrected for internal Faraday Rotation (see next section)*. Because the linear polarization becomes less reliable when the fractional polarization,  $S_P/S_I$ , falls below 0.5% (see Wiegert et al. 2015), we show the 0.5% fractional polarization contour in blue. Interior to that contour, the total intensity emission is very high so the fractional polarization is low and the results in that central

<sup>7</sup>These are actually electric field vectors rotated by 90 degrees.

region are unreliable. Outside of the blue contour where the polarization is reliable, systematic behaviour is seen over size scales of  $\approx 10$  arcsec (1.6 kpc) from the nucleus. There is emission to the east, west and north of the nucleus which are labelled in the figure. The west peak is at the location of the west extension seen in the total intensity image of Fig. 1.

The lower image shows the high resolution C-configuration map. Again, inside the blue contour, the polarization becomes unreliable. Thus, the two peaks closest to the galaxy's center (4 arcsec NW and SE of center) are not believable features. The most obvious reliable feature is the emission in the boxed region to the west of the nucleus with the appearance of a radio lobe, labelled 'west lobe'. This west lobe corresponds to the west peak labelled in the top image. The lobe broadens somewhat at its west end.

The north and east peaks, labelled in both images, are much less obvious in the high resolution (bottom) map. To compare, we have measured the flux density of the east peak in a region in which both maps have a percentage polarization  $> 0.5\%$ . The size of that region is  $1.26 \times$  the D-configuration beam size and  $11.8 \times$  the C-configuration beam size. The result is  $S_{D\text{-configuration}} = 75.3 \mu\text{Jy}$  and  $S_{C\text{-configuration}} = 69.5 \mu\text{Jy}$ , the latter only 8% lower. In these maps, some pixels are also blanked in the process of forming polarization images (Sect. 3.1). For C-configuration, these blanks occupy 1.5 beams (13% of the measured region). If flux exists at the Q and U rms level for those pixels, then the C-configuration flux density would increase to  $S_{C\text{-configuration}} = 74.0 \mu\text{Jy}$ , in close agreement with the D-configuration result. As for the weaker north peak, it is barely detected at high resolution. The *maximum* brightness at D-configuration is  $53.2 \mu\text{Jy}/\text{beam}$  which, with beam dilution (see Table 1), would result in  $4.3 \mu\text{Jy}/\text{beam}$  at C-configuration, i.e. a level of only  $1.5 \sigma$ . In summary, the differences between the configurations can be attributed to S/N and resolution differences between the two observations. The combined configuration data, presented in Sect. 4.2, will make use of both of these data sets and provide further revelations about the source structure.

The west radio lobe seen at C-configuration is quite distinct. For this feature, we have there-

fore formed a map of percentage polarization (greyscale) in Fig. 3 (top) with the unreliable regions blanked. Superimposed are red contours of linear polarization. The percentage polarization is 8.9% at its total intensity peak (at RA = 09 45 41.48, DEC = -14 19 30.5) and shows an increase towards the west end of the radio lobe. Average values for this lobe and other parameters are listed in Table 2.

For reference, we have also downloaded from the NASA/IPAC Extragalactic Database (NED) the high resolution  $1.4 \text{ GHz}$  total intensity image of Ulvestad & Wilson (1989) which shows structure associated with the inner double-loop in the region of our central oval. These data are represented by blue contours in Fig. 3. This high resolution map (as well as the CHANG-ES data sets, e.g. Fig. 1) shows quite clearly that the centre of the galaxy, as listed in NED and taken from the optical (photographic) data of Argyle & Eldridge (1990) (RA =  $09^{\text{h}} 45^{\text{m}} 42.^{\text{s}}05$ , DEC =  $-14^{\circ} 19' 34.''98$ ) is offset towards the east of the radio core by about 1 arcsec. The radio core is at RA =  $09^{\text{h}} 45^{\text{m}} 41.^{\text{s}}94$ , DEC =  $-14^{\circ} 19' 34.''8$ , with an estimated error of  $\pm 0.3$  arcsec in each coordinate. Clearly, the radio core provides the more accurate center position, but we have retained the NED center location mark in our images since this was our pointing center.

## 4.2. Results – Combined (C+D) Configurations

The low (10 arcsec) and high ( $\approx 4$  arcsec) resolution combined C+D configuration images are shown in Fig. 4 (top and bottom, respectively). The linearly polarized intensity is shown in greyscale and several total intensity contours at matching resolution are shown in white. The regions over which the percentage polarization falls below believable values is similar to those shown in Fig. 2. The magnetic field orientation *corrected for Faraday rotation* is now shown as red vectors. The corresponding RM maps are shown in Fig. 5.

Since the RM synthesis technique corrects for any foreground Faraday rotation, both in the galaxy as well as Galactic, the magnetic field orientation shown in Fig. 4 is intrinsic to NGC 2992. The Galactic contribution to this foreground is estimated to be  $-13 \pm 13 \text{ rad/m}^2$  at the location of NGC 2992 (Oppermann et al. 2012), consistent

with zero. However, taking the measurements at face value, the Galactic contribution would be 1.8 degrees for the band center of NGC 2992 or a maximum of 2.7 degrees for the lowest frequency.

The results discussed in Sect. 4.1 are still valid but now further clarity has been achieved, with the main new results being revealed in Fig. 4 (top). The north peak, as labelled in Fig. 2 (top) is now seen as belonging to emission along the galaxy's major axis which runs NNE to SSW (Fig. 1) and, in addition, emission is now also seen along the SSW major axis. Most dramatically, the west and east peaks of Fig. 2 are now revealed as *two radio lobes on either side of the major axis* (see also Fig. 6). As we saw before in Fig. 2 (bottom), the west lobe is the more compact one and can be seen distinctly as the discrete radio lobe in Fig. 4 (bottom).

The magnetic field vectors, once corrected for Faraday rotation, (as they did before) show ordered fields predominantly pointing roughly away from the galaxy's center (and AGN) but the vectors appear to show some curvature 'around' the eastern radio lobe (Fig. 4 top). It is the eastern radio lobe that extends farthest from the AGN and is not as compact or as bright as the western lobe. It also appears to have escaped from the galaxy's disk (see also Fig. 6). The B vectors are very straight in this escaping part of the eastern radio lobe. Along the northern and southern major axes, there is also some curvature away from the plane of the galaxy.

In the high resolution image (Fig. 4 bottom), the corrected magnetic field vectors are seen to curve along the western radio lobe with the curvature being somewhat more pronounced than previously seen in Fig. 2 (bottom). We again produce a map of percentage polarization for the discrete western radio lobe (Fig. 3 bottom) which, as before, shows the increase in the percentage polarization towards the west end of this feature.

In summary, a comparison of Figs. 2 and 6 shows that ordered magnetic fields are apparent and the overall sense of that order is evident and consistent in both cases. However Faraday rotation corrections should not be neglected at C-band; for example after correction, the magnetic field shows more curvature in the west radio lobe. Configuration combination also illustrates the radio lobes much more clearly. A comparison of

the percentage polarization (Fig. 3) before (top) and after (bottom) configuration combination and Faraday rotation correction also shows consistent results, especially the higher percentage polarization (higher contribution of the ordered magnetic field) towards the end of the west radio lobe.

### 4.3. X-ray Observations of NGC 2992

Multiple CHANDRA observations were carried out for NGC 2992 with the Advanced CCD Imaging Spectrometer-Spectroscopy (ACIS-S) at the focus. One of these observations was taken without the High Energy Transmission Gratings (HETG). We find that the AGN in the image of this observation is strongly saturated. This problem is minimized in observations with the HETG.

In Fig. 7 we show only an image in the 0.5-4 keV band in colour, constructed with the longest ACIS-S/HETG 0th-order exposure (OB #11858) of 95 ks; the additional 41 ks from the other two observations would not change the image quality in any significant way. The data have been adaptively smoothed with the *csmooth* routine of the CIAO (Chandra Interactive Analysis of Observations<sup>8</sup>) software analysis package. Superimposed are C-configuration C-band total intensity contours in grey (as in Fig. 1) and the C-configuration C-band linearly polarized contours (as in Fig. 2 bottom).

Closest to the galaxy's center, the X-ray emission (white part plus red contours) is enhanced NNE/SSW which is in the direction of the galaxy's disk. In the X-ray, the NNE/SSW orientation continues to larger scales, especially towards the SW; these features are still along and within the confines of the optical disk as shown in Fig. 1. The CHANDRA image clearly shows the AGN (center of the highest red contour), and its position corresponds within errors to the radio peak (Sect. 4.1) rather than the NED center.

In addition to the AGN, the CHANDRA image shows the presence of the apparently diffuse X-ray emission; note that the X-ray emission is uncorrected for the dust lane which lies approximately between the central X-ray peak and the polarized western radio lobe. The lack of any direct evidence for an X-ray and radio jet may indicate that the radio lobes represent a relic of an earlier episode of the AGN (see Sect. 5.1).

<sup>8</sup> <http://cxc.harvard.edu/ciao/>



## 5. Discussion

The key results of this paper are that linearly polarized emission has revealed a double-lobed radio source along the minor axis (east-west) direction of NGC 2992 that is masked in total intensity emission, and that the western lobe is seen as a very discrete radio lobe at high resolution. Clearly, these polarized structures have been masked by the stronger unpolarized emission.

There are two other good examples in the CHANG-ES sample of known AGNs with distinct radio lobes for which lobes are much more obvious in polarization than in total intensity, namely NGC 3079 (Wiegert et al. 2015) and NGC 4388 (Wiegert et al. 2015; Damas-Segovia et al. 2016). We show the previously unpublished total intensity and polarized image of NGC 3079 in Fig. 8. Details related to this galaxy will be discussed elsewhere, but this is another example in which the outflow, in particular the radio lobe to the east, is much more obvious in polarization. The peak total intensity emission (top image) occurs at the nucleus rather than in the east lobe. The brightness ratio of east radio lobe to nucleus (both measured at their respective peaks) is only 0.58. By contrast, for the linearly polarized emission (bottom), the east radio lobe is brightest, with an east lobe to nucleus ratio of 5.8. In other words, the contrast has increased by a factor of 10. Similar results can be seen in NGC 4388 (see Damas-Segovia et al. 2016). In both NGC 3079 and NGC 4388, the nuclear outflow is strong enough that the radio lobes can also be seen in total intensity, whereas this is not the case for NGC 2992.

### 5.1. AGN-Related Outflow

The evidence for an AGN in NGC 2992 has been outlined in Sect. 2 and the case for AGN-related outflow has also been made; for example Veilleux et al. (2001) indicate that the most likely energy source for the optical outflow is a hot, bipolar, thermal wind powered by the AGN and diverted along the galaxy’s minor axis by the pressure gradient of the ISM. In this section, we provide further evidence that the outflow is predominantly AGN-related.

Firstly, the discrete western radio lobe seen at high resolution in NGC 2992 (Fig. 3) has the appearance of most extragalactic radio lobes

(EGRLs) seen in distant galaxies, though is small-scale in comparison, extending to 1.6 kpc from the galaxy’s center. It is similar to what has been seen before for Seyferts and other galaxies that show radio lobes in total intensity (Sect. 1).

Outflows are also known to result from nuclear starbursts and SNe in starbursts can be more effective at driving galactic-scale winds than AGN (Strickland 2004) in LLAGNs. Such winds are dominated by hot gas, visible in X-ray emission and in H $\alpha$  (e.g. Heesen et al. 2011, and references therein). However, these winds (such as are known) are in conical outflows. They also align with the galaxies’ minor axes, *even at the smallest scales*, i.e. as soon as the outflow leaves the SF region, because the alignment is a result of the surrounding ISM which focusses the outflow and causes it to move in the direction of steepest pressure gradient (e.g. Strickland 2004). For the starburst-driven wind in NGC 253, both the total intensity as well as the polarized radio emission are also filamentary and surround the nuclear outflow which is collimated by a helical magnetic field into a wide-angle cone (Heesen et al. 2011). In M 82, the radio emission is also observed along the outside of the wind (Adebahr et al. 2013). In general, starburst-related winds have opening angles of 10 to 45 deg. near the base increasing to 45 to 100 deg. above the disk (Veilleux et al. 2005) for those systems that are well-known.

The distinct western lobe in NGC 2992, by contrast, appears more ‘lobe-like’ than ‘cone-like’ in these observations. It is also *mis-aligned* with the galaxy’s center. Fig. 3 illustrates this best in which we have shown high resolution 1.4 GHz contours from the inner double-loop (Ulvestad & Wilson 1989) which is in our inner central oval location. The orientation of the inner double-loop is strongly misaligned with the minor axis and is well-known to represent ejection from the AGN. The western radio lobe then becomes aligned with the minor axis. These observations suggest that outflow near the nucleus first extends towards the NNW and then it curves towards the west (the direction of the minor axis) as expected from ISM pressure gradients. On larger scales towards the east and west (Fig. 6 the alignment is roughly along the minor axis.

Ordered magnetic fields are also typical of aligned outflows from AGNs. In EGRLs, magnetic

field alignments and their causes are still debated (e.g. Tucci & Toffolatti 2012). However, in classic aligned outflow, the radial component of the field would fall off as  $1/r^2$ , since flux is conserved and the radial component declines with increasing cross-sectional area. A helical field wrapping around the outflow would decline as  $1/r$ , that is, as the circumference. Consequently, one would expect  $B$  to align parallel to the jet close to the origin, as many such observations show (Cawthorne et al. 1993; Gómez et al. 2008), but once the circumferential field starts to dominate,  $B$  would become perpendicular farther from the origin, as is sometimes, but not always observed (Schwartz et al. 2000). Alternatively,  $B$  parallel to the outflow axis may result if the initial fields are sheared to lie in a plane. Strong shocks can compress an initially random field, creating an ordered magnetic field, in which case transverse magnetic field vectors would result in the region of the shocks (Tucci & Toffolatti 2012). Radio knots are generally interpreted as the termination point of a jet that is stopped in the dense ISM where the radio emission is enhanced by compressed material and magnetic fields (Falcke et al. 1998; Leipski et al. 2006).

In the case of the west lobe of NGC 2992 (Fig. 4 bottom), we observe curving magnetic fields. The curvature appears to follow the direction that the radio lobe, itself, would be bending because of pressure gradients in the ISM. The fields become somewhat more transverse at the west (terminating) end, similar to the EGRLs just described. An increase in percentage polarization towards the end of the lobe (Fig. 3) is consistent with this interpretation<sup>9</sup>.

From optical emission lines, there is also much evidence for radial flows including cone-like outflow (Veilleux et al. 2001) towards the east and west. Our total intensity image (Fig. 1) as well as our low-resolution polarization images that show magnetic fields pointing radially away from the nucleus (Fig. 4 top) agree with this picture that on

<sup>9</sup>Note that Hanasz et al. (2009) show that organized magnetic fields can be set up in galaxies within 2 Gyr of disk evolution from initially randomly oriented exploding magnetized stars; that is, organized fields can occur without any outflow. However, such fields are on a global scale and cannot explain embedded structures such as are observed here.

larger scales, we can see wider outflow. A detailed comparison of the optical and radio outflows is beyond the scope of this paper. However, we do note that the distinct west radio lobe is located within the western optical cone in projection. Finally, Friedrich et al. (2010) have shown, on energetic grounds, that outflows on scales up to 2 kpc cannot have been produced by a starburst and must have originated with the AGN. This is approximately the same spatial scale over which we see the radio lobe.

In summary, the weight of evidence indicates that we are observing embedded weak polarized radio lobes that originate with an AGN in NGC 2992.

## 5.2. Interaction with the ISM and Physical Parameters

It is clear that the radio lobes are interacting with the ISM. On the west side, the lobe has not yet escaped from the galaxy but the east lobe has emerged outside of the disk. The discrete west lobe of NGC 2992, as discussed above, does not align directly with the nucleus (Fig. 3) and, if the AGN-related outflow has maintained its direction over time, then there has been a significant bend in the outflow direction between 3 and 7 arcsec from the nucleus ( $\approx 500 - 1200$  pc in projection). Such bends are also commonly seen in EGRLs, for a variety of reasons (e.g. precessing jets, Kelvin-Helmholtz instabilities, etc.) but for NGC 2992, the bend is more likely caused by a deflection due to pressure gradients in the ISM as described in early models such as Henriksen, Vallée, & Bridle (1981); Fiedler & Henriksen (1984). Similar bending has been observed before in spiral galaxies, e.g. in NGC 4258 (Plante et al. 1991; Krause et al. 2007).

Measured and derived properties of the distinct western radio lobe of NGC 2992 are listed in Table 2 measured within the  $3\sigma$  contour as shown in Fig. 3 (top).

The percentage polarization is significant, i.e.  $\approx 6\%$ . This value may, however, be underestimated. This is because we do not observe the radio lobes in total intensity and have simply measured the total intensity over a region that corresponds to the observed polarized radio lobe. Consequently, the total intensity measurement could

include any other total intensity emission along the line of sight that is outside of the radio lobe itself, thus increasing  $S_I$  in comparison to  $S_P$ <sup>10</sup>. As a comparison, in distant EGRLs, values are only a few percent at this frequency (Tucci & Toffolatti 2012, and references therein), possibly because of poorer linear resolution for the more distant sources (but see also Bagchi et al. (2007)). However, higher percentages have been seen in other nearby spiral galaxies, for example the similar galaxy, NGC 4388 (Damas-Segovia et al. 2016).

In Table 2, we also provide the minimum energy magnetic field<sup>11</sup>; this was determined from the total intensity flux density, following Beck & Krause (2005), assuming that the measured spectral index  $\approx$  the non-thermal spectral index. If the spectral index steepens by 10% due to a thermal contribution, then  $B_{min}$  increases by +4%. If the line of sight distance decreases by a factor of 2, then  $B_{min}$  will increase by 18→20%. The same cautions outlined in the previous paragraph apply here.

The minimum total field value (Table 2), if random, suggests a magnetic pressure of  $5 \times 10^{-11}$  erg cm<sup>-3</sup>. By comparison, typical values for galactic disks are  $10^{-11}$  erg cm<sup>-3</sup> (e.g. Beck 2007, 2015) and are about 3 times larger in the central regions. Consequently, the value is high enough that the jet should propagate but not so high that it wouldn't be affected by the surrounding ISM, as the changes in orientation suggest. As further confirmation, Colbert et al. (2005) indicate that, within the central 5 arcsec, the pressure of the X-ray emitting gas is  $\phi_X^{-1/2}(0.5 - 3) \times 10^{-11}$  erg cm<sup>-3</sup>, where  $\phi_X$  is the volume filling factor, and they also indicate that this value is similar to the extended narrow line region clouds. Consequently, pressure calculations from a wide variety of observations are all pointing to values that are within factors of a few, of order several  $10^{-11}$  erg cm<sup>-3</sup>.

With sufficient data, it should be possible to make use of such observations to determine (or place limits on) the physical conditions in a galaxy,

or the energetics of the outflow, or both. For example, the 'stall' location of a radio lobe should occur where the lobe pressure equals the ISM pressure, and a lobe should emerge from the disk if its pressure exceeds that of the ISM (as for the east lobe of NGC 2992). The relation between the intrinsic bending angle and jet ram pressure is also known for environments with static atmospheres (Henriksen, Vallée, & Bridle 1981; Irwin & Seaquist 1988). Since NGC 2992 has been well-observed at a variety of wavelengths (Sect. 2), this galaxy should be well-suited to the development of a detailed model that includes the X-ray, optical and other data that are available.

### 5.3. A Possible Evolutionary Scenario

The simplest scenario that is consistent with the data presented here (although it is not a unique interpretation), is that the AGN outflow in NGC 2992 has been episodic but not changing direction at the source, or that episodic outflows are embedded within steadier low level emission.

For example, the most recent activity would belong to the total intensity inner double-loop region within our inner oval region (Fig. 1) and oriented NNW-SSE. We would not see this outflow explicitly in linear polarization because the percentage polarization is below believable levels near the galaxy's center.

At an earlier time, the higher resolution western radio lobe observed in linear polarization was formed and the observed polarized feature would therefore be a relic of this earlier activity. Pressure gradients in the ISM cause this outflow to bend towards the minor axis. The low resolution eastern and western radio lobes could have occurred at approximately the same time or else they represent lower level continuous flows (e.g. note that the B vectors don't curve around the lobes as is sometimes seen in EGRLs). Since NGC 2992 is highly disturbed because of the interaction with its companions, the eastern disk could have a different ISM pressure gradient, allowing the eastern lobe to escape from the disk as observed. These features would not be seen in total intensity because the broader scale total intensity emission is much brighter, masking the polarized intensity structure.

<sup>10</sup>Free-free emission is also present but is a minor contributor to total intensity in comparison with non-thermal emission.

<sup>11</sup>Although we cannot verify that the minimum energy criterion strictly applies, it is the only way to obtain such quantities and presents a baseline for possible future comparisons.

TABLE 2  
PARAMETERS OF THE NGC 2992 WEST RADIO LOBE<sup>a</sup>

Observation	$S_I^b$ (mJy)	$S_P^b$ ( $\mu$ Jy)	$SP_I^c$ ( $\times 10^{19}$ W Hz <sup>-1</sup> )	$SP_P^c$ ( $\times 10^{19}$ W Hz <sup>-1</sup> )	$\overline{P/I}^d$ (%)	$\bar{\alpha}^e$	$B_{min}^f$ ( $\mu$ G)	$P_B^g$ ( $\times 10^{-11}$ erg cm <sup>-3</sup> )
<b>West lobe</b>	$2.21 \pm 0.03$	$97 \pm 2$	$30.6 \pm 0.4$	$1.34 \pm 0.03$	$6.4 \pm 0.2$	$-0.85 \pm 0.16$	35.6	5.0

<sup>a</sup>Measurements for the radio lobes seen in the C-configuration image of Fig. 3 (bottom). All measurements apply to the regions within the  $3\sigma$  contours, and where the fractional polarization has an unblanked value.

<sup>b</sup>Flux densities of the total intensity emission and the linearly polarized emission. The uncertainty estimate reflects variations that result from varying the irregularly sized measurement region, whose value dominates over the error calculated from the rms noise values given in Table 1.

<sup>c</sup>Spectral power of the total intensity and polarized emission.

<sup>d</sup>Average fractional polarization measured from Fig. 3.

<sup>e</sup>Average total intensity spectral index ( $S_\nu \propto \nu^\alpha$ ) and its error from maps (not shown) generated as described in Wiegert et al. (2015).

<sup>f</sup>Minimum energy (total) magnetic field computed according to the prescription of Beck & Krause (2005) assuming the number density ratio of protons to electrons per unit energy,  $K_0 = 100$ , the line of sight distance is equal to the width of the feature, and using values of  $S_I$  and  $\alpha$  in this table. See Sect. 5 for estimates of some uncertainties.

<sup>g</sup>Magnetic pressure, assuming random fields ( $P_B = B_{min}^2/8\pi$ ).

Finally, the southeast extension (Fig. 1) would belong to an even earlier episode. This feature has emerged from the galaxy and is pointing towards the companion galaxy, NGC 2993. Polarized emission would not be seen from this extended feature because it is just too weak on this larger scale.

Since the optical emission appears as a wide-angled cone (Allen et al. 1999) with the west radio lobe within it in projection, the discrete radio features may represent specific high-energy ejection episodes in comparison to lower level steady emission. The latter is more likely explained by an AGN-powered thermal wind as described in Veilleux et al. (2001).

## 6. Conclusions

The polarized emission from NGC 2992, uniquely provided by the CHANG-ES survey, has offered us a new glimpse into the nuclear activity in this galaxy. Although radio lobes are *not* observed in total intensity radio emission, they *are* observed in polarized emission. Thus, we are observing weak radio lobes which were not strong enough to be distinguished from other non-polarized emission seen in total intensity.

For NGC 2992, at high resolution, a single discrete radio lobe is observed on the western side of the galaxy's center and at low resolution, two radio lobes are seen on either side of the nucleus, extending to the east and west. The eastern radio lobe has emerged from the galaxy whereas the western lobe is within the disk. We argue that the radio lobes are consistent with AGN-like out-

flow. The orientation of the discrete western radio lobe is consistent with outflow that has been redirected, via pressure-gradients in the ISM, along the minor axis. The outflow and ISM pressures are consistent with this picture, to within measurable factors of a few (assuming that the minimum energy criterion holds).

We suggest a possible (though not unique) evolutionary scenario for the observed radio features such that the variety of radio activity seen in this galaxy can be simply explained by episodic outflow from the AGN, possibly embedded within more steady lower level flows. The AGN is at the radio core position which should designate the center of the galaxy, rather than the normally quoted optical center.

Such polarized radio lobes provide a unique opportunity to study the physics of outflow/ISM interactions in spiral galaxies with LLAGNs.

This work has been supported by a Discovery Grant to the first author by the Natural Sciences and Engineering Research Council of Canada. This research has made use of the NASA/IPAC Extragalactic Database (NED) which is operated by the Jet Propulsion Laboratory, California Institute of Technology, under contract with the National Aeronautics and Space Administration. The National Radio Astronomy Observatory is a facility of the National Science Foundation operated under cooperative agreement by Associated Universities, Inc. We thank Dominic Schnitzeler for his helpful comments to improve this paper.

*Facilities: VLA.*

## REFERENCES

- Adebahr, B., Krause, M., Klein, U., Weźgowiec, M., Bomans, D. J., & Dettmar, R.-J. 2013, *A&A*, 555, A23
- Allen, M. G., Dopita, M. A., Tsvetanov, Z. I., & Sutherland, R. S. 1999, *ApJ*, 511, 686
- Argyle, R. W., & Eldridge, P. 1990, *MNRAS*, 243, 504
- Bagchi, J., Gopal-Krishna, Krause, M., & Joshi, S. 2007, *ApJ*, 670, L85
- Bagchi, J., Vikram, V. M., Hota, A., et al. 2014, *ApJ*, 788, 174
- Baldwin, J. A., Phillips, M. M., & Tavelich, R. 1981, *PASP*, 93, 5
- Beck, R., & Krause, M. 2005, *Astron. Nachr.*, 326, 414
- Beck, R. 2007, *A&A*, 470, 539
- Beck, R. 2015, *A&A*, 578A, 93
- Beck, R., & Wielebinski, R. 2013, in *Planets, Stars and Stellar Systems*, Vol. 5, ed. T. D. Oswalt, & G. Gilmore, Springer Science+Business Media, Dordrecht, pp. 641 - 723
- Beckmann, V., Gehrels, N., & Tueller, J. 2007, *ApJ*, 666, 122
- , Brentjens, M. A., & de Bruyn, A. G. 2005, *A&A*, 441, 1217
- Briggs, D. S. 1995, *High Fidelity Deconvolution of Moderately Resolved Sources*, PhD Thesis, The New Mexico Institute of Mining and Technology, Socorro, NM
- Cawthorne, T. V., Wardle, J. F. C., Roberts, D. H., & Gabuzda, D. C. 1993, *ApJ*, 416, 519
- Chapman, S. C., Morris, S. L., Alonso-Herrero, A., & Falcke, H. 2000, *MNRAS*, 314, 263
- Colbert, E. J. M., Baum, S. A., Gallimore, J. F., et al. 1996, *ApJS*, 105, 75
- Colbert, E. J. M., Baum, S. A., O'Dea, C. P., & Veilleux, S. 1998, *ApJ*, 496, 786
- Colbert, E. J. M., Strickland, D. K., Veilleux, S., & Weaver, K. A. 2005, *ApJ*, 628, 113
- Colina, I., Fricke, K. J., Kollatschny, W., & Per-ryman, M. A. C. 1987, *A&A*, 178, 51
- Cornwell, T. J. 2008, *IEEE J. of Selected Topics in Signal Proc.*, Vol. 2, No. 5, 793
- Cornwell, T. J., Golap, K., & Bhatnagar, S. 2008, *IEEE J. of Selected Topics in Signal Proc.*, Vol. 2, No. 5, 647
- Damas-Segovia, A., Beck, R., Vollmer, B., et al. 2016, *ApJ*, 824, 30 (CHANG-ES VII)
- Dasyra, K. M., Bostrom, A. C., Combes, F., & Vlahakis, N. 2015, arXiv:150305484
- Duc, P.-A., Brinks, E., Springel, V., et al. 2000, *AJ*, 120, 1238
- Dotti, M., Colpi, M., Pallini, S., et al. 2013, *ApJ*, 762, 68
- Elvis, M., Fassnacht, C., Wilson, A. S., & Briel, U. 1990, *ApJ*, 361, 459
- Everett, J. E., & Weisberg, J., M. 2001, *ApJ*, 553, 341
- Falcke, H., Wilson, A. S., & Simpson, C. 1998, *ApJ*, 502, 199
- Ferrarese, L., & Merritt, D. 2000, *ApJ*, 539, L9
- Fiedler, R., & Henriksen, R. N. 1984, *ApJ*, 281, 554
- Friedrich, S., Davies, R. I., Hicks, E. K. S., et al. 2010, *A&A*, 519, 79
- Garcia-Lorenzo, B., Arribas, S., & Mediavilla, E. 2001, *A&A*, 378, 787
- Gebhardt, K., Bender, G., Bower, A., et al. 2000, *ApJ*, 539, L13
- Gilli, R., Maiolino, R., Marconi, A., et al. 2000, *A&A*, 355, 485
- Glass, I. S. 1997, *MNRAS*, 292, L50
- Gómez, J. L., Marscher, A. P., Jorstad, S. G., et al. 2008, *ApJ*, 681, 69
- Greenhill, L. J., Jiang, D. R., Moran, J. M., et al. 1995, *ApJ*, 440, 619

- Greenhill, L. J., et al. 2003, ApJ, 440, 619
- Hanasz, M., Woltanski, D., & Kowalik, K. 2009, ApJ, 706, L155
- Harnett, J. I., Whiteoak, J. B., Reynolds, J. E., Gardner, F. F., & Tzioumis, A. 1990, MNRAS, 244, 130
- Heald, G., Braun, R., & Edmonds, R. 2009, A&A, 503, 409
- Heesen, V., Beck, R., Krause, M., & Dettmar, R.-J. 2011, A&A, A79
- Henriksen, R. N., Vallée, J. P., & Bridle, A. H. 1981, ApJ, 249, 40
- Herrnstein, J. R., Moran, J. M., Greenhill, L. J., et al. 1998, ApJ, 508, 243
- Ho, L. C., & Ulvestad, J. S. 2001, ApJS, 133, 77
- Hota, A., Sirothia, S. K., Ohyama, Y., et al. 2011, MNRAS, 417, L36
- Hummel, E., van Gorkom, J. H., & Kotanyi, C. G. 1983, ApJ, 267, L5
- Irwin, J. A., & Seaquist, E. R. 1988, ApJ, 335, 658
- Irwin, J. A., Beck, R., Benjamin, R. A., et al. 2012a, AJ, 144, 43 (CHANG-ES I)
- Irwin, J. A., Krause, M., English, J., et al. 2013, AJ, 146, 164 (CHANG-ES III)
- Kaviraj, S., Shabala, S. S., Deller, A. T., & Middelberg, E. 2015, MNRAS, 452, 774
- Kaviraj, S., Shabala, S. S., Deller, A. T., & Middelberg, E. 2015, MNRAS, 454, 1595
- Keel, W. C., White, R. E., Owen, F. N., & Ledlow, M. J. 2006, AJ, 132, 2233
- Kirkpatrick, A., Pope, A., Sajina, A., et al. 2015, ApJ, 814, 9
- Kormendy, J., & Ho, L. C. 2013, ARA&A, 51, 511
- Krause, M., Fendt, C., & Neininger, N. 2007, A&A, 467, 1037
- Krause, M., & Löhner, A. 2004, A&A, 420, 115
- Kruper, J. S., Urry, C. M., & Canizares, C. R. 1990, ApJS, 74, 347
- Laine, S., & Beck, R. 2008, ApJ, 673, 128
- Laor, A. 2000, ApJ, 543, L111
- Ledlow, M. J., Owen, F. N., Yun, M. S., & Hill, J. M. 2001, ApJ, 552, 120
- Leipski, C., Falcke, H., Bennert, N., & Hüttemeister, S. 2006, A&A, 455, 161
- Li, J.-T., Beck, R., Dettmar, R.-J., et al. 2016, MNRAS, 456, 1723 (CHANG-ES VI)
- Maccacaro, T., Perola, G. C., & Elvis, M. 1982, ApJ, 257, 47
- Mao, M., Owen, F., Duffin, R., et al. 2015, MNRAS, 446, 4176
- Marquez, I., Boisson, C., Durret, F., & Petitjean, P. 1998, A&A, 333, 459
- Márquez, I., & the Degas Consortium, 2003, EAS Publications Series, Volume 10, *Galactic and Stellar Dynamics*, Proceedings of JENAM 2002, held in Porto, Portugal, 3-6 September, 2002. Ed. C. M. Boily, P. Patsis, S. Portegies Zwart, R. Spurzem and C. Theis, pp.17.
- McMullin, J. P., et al. 2007, Astronomical Data Analysis Software and Systems XVI, ASP Conf. Series, Vol. 376, Ed., R. A. Shaw, F. Hill, & D. J. Bell, p. 127
- Miyoshi, M., Moran, J., Herrnstein, J., et al. 1995, Nature, 373, 127
- Mushotsky, R. 2004, in Supermassive Black Holes in the Distant Universe, ed. Amy J. Barger, Kluwer Academic Publishers, Dordrecht, The Netherlands, p.53
- Narayan, R., & Hi, I. 1995, ApJ, 452, 710
- Oppermann, N., Junklewitz, H., Robbers, G., et al. 2012, A&A, 542, 93
- Osmer, P. S., Smith, M. G., & Weedman, D. W., ApJ, 192, 279
- Pereira-Santaella, M., Diamond-Stanic, A. M., Alonso-Herrero, A., & Rieke, G. H. 2010, ApJ, 725, 2270
- Plante, R. L., Lo, K. Y., Roy, J.-R., & Martin, P. 1991, ApJ, 381, 110

- Rau, U., & Cornwell, T. J. 2011, *A&A*, 532, A71
- Schwartz, D. A., Marshall, H. L., Lovell, J. E. J., et al. 2000, *ApJ*, 540, 69
- Shafi, N., Oosterloo, T. A., Morganti, R., et al. 2015, *MNRAS*, 454, 1404
- Shu, X. W., Yaqoob, T., Murphy, K. D., et al. 2010, *ApJ*, 713, 1256
- Sikora, M., Stawarz, L., & Lasota, J.-P. 2007, *ApJ*, 658, 815
- Sikora, M., & Begelman, M. C. 2013, *ApJ*, 764, 24
- Simmons, J. F. L., & Stewart, B. G., *A&A*, 142, 100
- Strickland, D. K. 2004, *The Interplay among Black Holes, Stars and ISM in Galactic Nuclei*, Proc. IAU Symposium, 222, Eds. T. Storchi-Bergmann, L. C. Ho, & H. R. Schmitt, 249
- Tchekhovskoy, A., Narayan, R., & McKinney, J. C. 2010, *ApJ*, 711, 50
- Trippe, M. L., Crenshaw, D. M., Deo, R., & Dietrich, M. 2008, *AJ*, 135, 2048
- Tsvetanov, Z., Dopita, M., & Allen, M. *BAAS*, 27, 871
- Tucci, M., & Toffolatti, L. 2012, *Advances in Astronomy*, 2012, 52
- Ulvestad, J. S., & Wilson, A. S. 1984, *ApJ*, 285, 439
- Ulvestad, J. S., & Wilson, A. S. 1989, *ApJ*, 343, 659
- Vaillancourt, J. E. 2006, *PASP*, 118, 1340
- Veilleux, S., Shopbell, P. L., & Miller, S. T. 2001, *AJ*, 121, 198
- Veilleux, S., Cecil, G., & Bland-Hawthorn, J. 2005, *ARA&A*, 43, 769
- Ward, M., Penston, M. V., Blades, J. C., & Turtle, A. J. 1980, *MNRAS*, 193, 563
- Weaver, K. A., Nousek, J., Yaqoob, T., et al. 1996, *ApJ*, 458, 160
- Wehrle, A. E., & Morris, M. 1988, *AJ*, 95, 6
- Wiegert, T., Irwin, J., Miskolczi, A., et al. 2015, *AJ*, 150, 81 (CHANGES-IV)
- Wilson, A. S., & Colbert, E. J. M. 1995, *ApJ*, 438, 62
- Yuan, F., & Narayan, R. 2014, *ARA&A*, 52, 529
- Zheng, X. Z., Bell, E. F., Somerville, R. S., et al. 2009, *ApJ*, 707, 1566

---

This 2-column preprint was prepared with the AAS L<sup>A</sup>T<sub>E</sub>X macros v5.2.

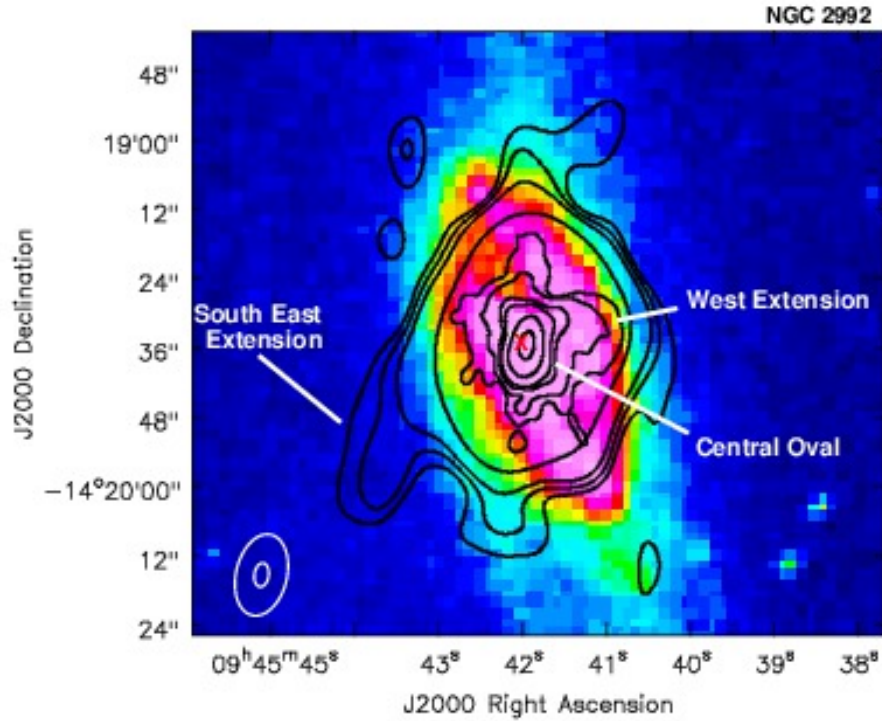


Fig. 1.— C-band total intensity contours on a Digitized Sky Survey (DSS2) blue image of NGC 2992. The four outermost contours are D-configuration data with contour levels at  $0.05$  ( $6\sigma$ ),  $0.07$ ,  $0.1$ , and  $0.3$   $\text{mJy beam}^{-1}$ ; the peak D specific intensity is  $65.6$   $\text{mJy beam}^{-1}$ . The inner six contours are C-configuration data with levels of  $0.035$  ( $10\sigma$ ),  $0.1$ ,  $0.5$ ,  $1.0$ ,  $5.0$ , and  $20$   $\text{mJy beam}^{-1}$ ; the peak C-configuration specific intensity is  $28.0$   $\text{mJy beam}^{-1}$ . The two beam sizes, both robust 0 weighting (Table 1) are shown at lower left and the galaxy NED center is marked with a red X. Several features mentioned in the text are labelled.



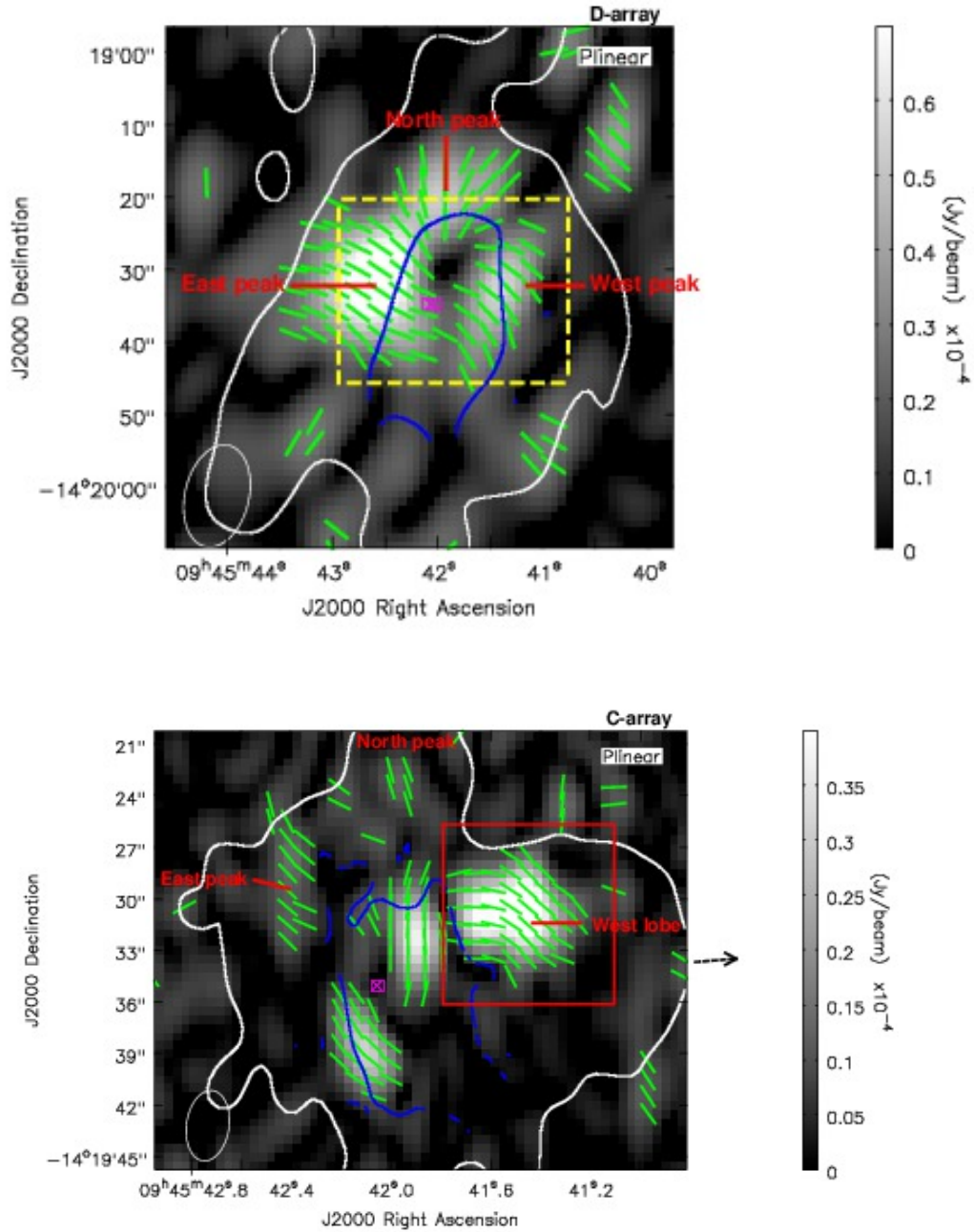


Fig. 2.— C-band linear polarization maps of NGC 2992 with apparent magnetic field vectors superimposed in green. *These vectors have not been Faraday de-rotated.* At **top** is the D-configuration data and at **bottom** is the C-configuration data (note the different map scales). The single white contour shows the corresponding total intensity  $6\sigma$  contour from Fig. 1. The yellow dashed box (top) shows the approximate field of view that is shown in the bottom image. The red box (bottom) shows the lobe-like feature discussed in the text. The interior of the blue contours represents where the fractional polarization falls below the believable 0.5% level. The NED (optical) center of the galaxy is marked with a magenta X in a box and the beams are shown at lower left. Several features discussed in the text are labelled and the approximate direction of the minor axis of the galaxy is shown with a dashed arrow towards the right in the bottom image.

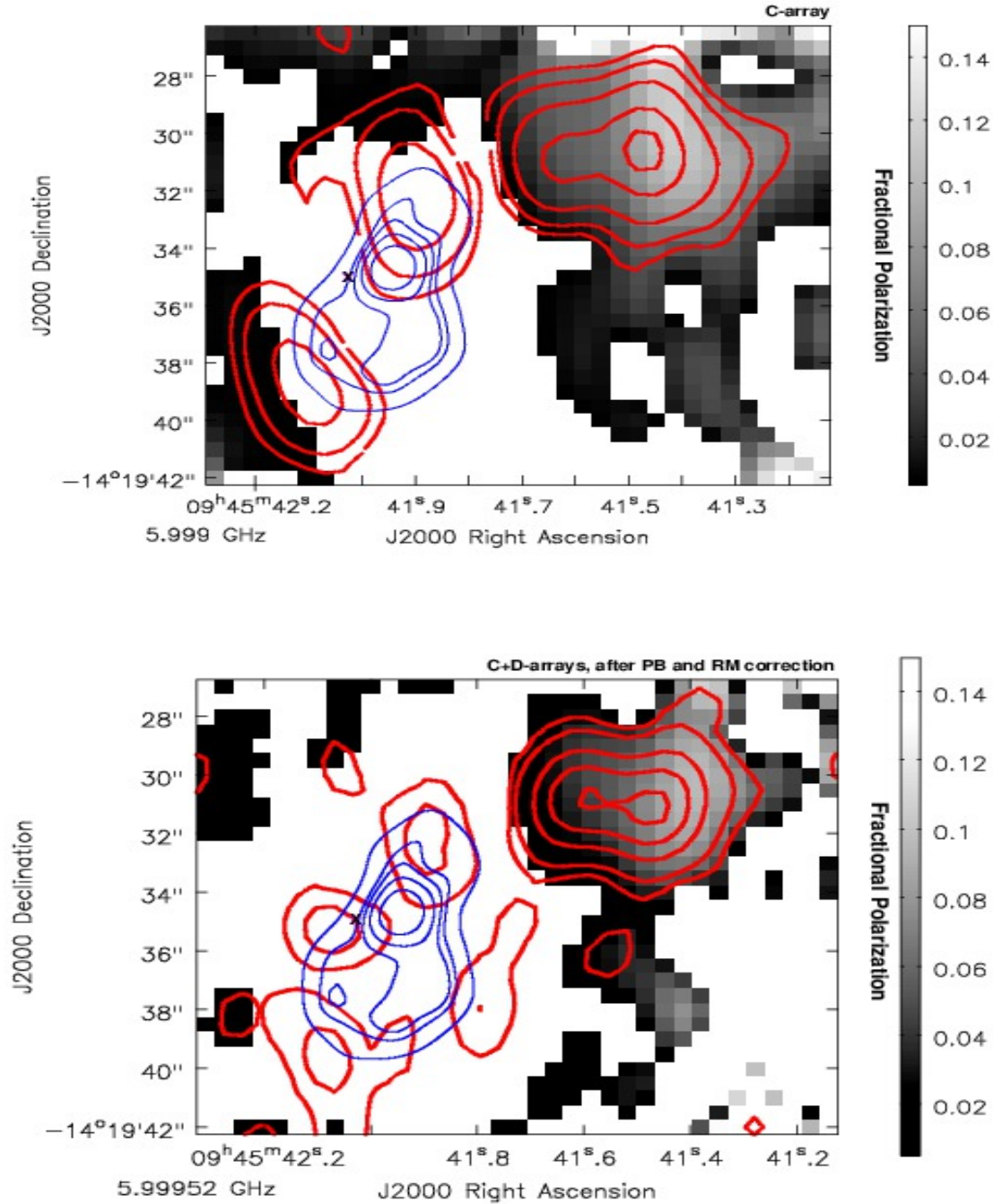


Fig. 3.— Fractional polarization (greyscale) with linear polarization contours superimposed in red. Blanked (white) regions are where the fractional polarization falls below 0.5%. The C-configuration data are shown at the **top** (not PB-corrected) with contours in red at 9.6 ( $3\sigma$ ), 15, 25, 40, and 50  $\mu\text{Jy}/\text{beam}$ . The high resolution combined C+D configuration data (PB-corrected) are at the **bottom** with contours in red at 15, 25, 40, 50, and 58  $\mu\text{Jy}/\text{beam}$ . Blue contours show the 1.4 GHz high resolution (1.7 x 1.2 arcsec at -17 deg) total intensity contours of the inner double-loop from Ulvestad & Wilson (1989), at levels of 5, 10, 12, 15, and 20  $\text{mJy beam}^{-1}$ . The NED center of the galaxy is marked with a small X.

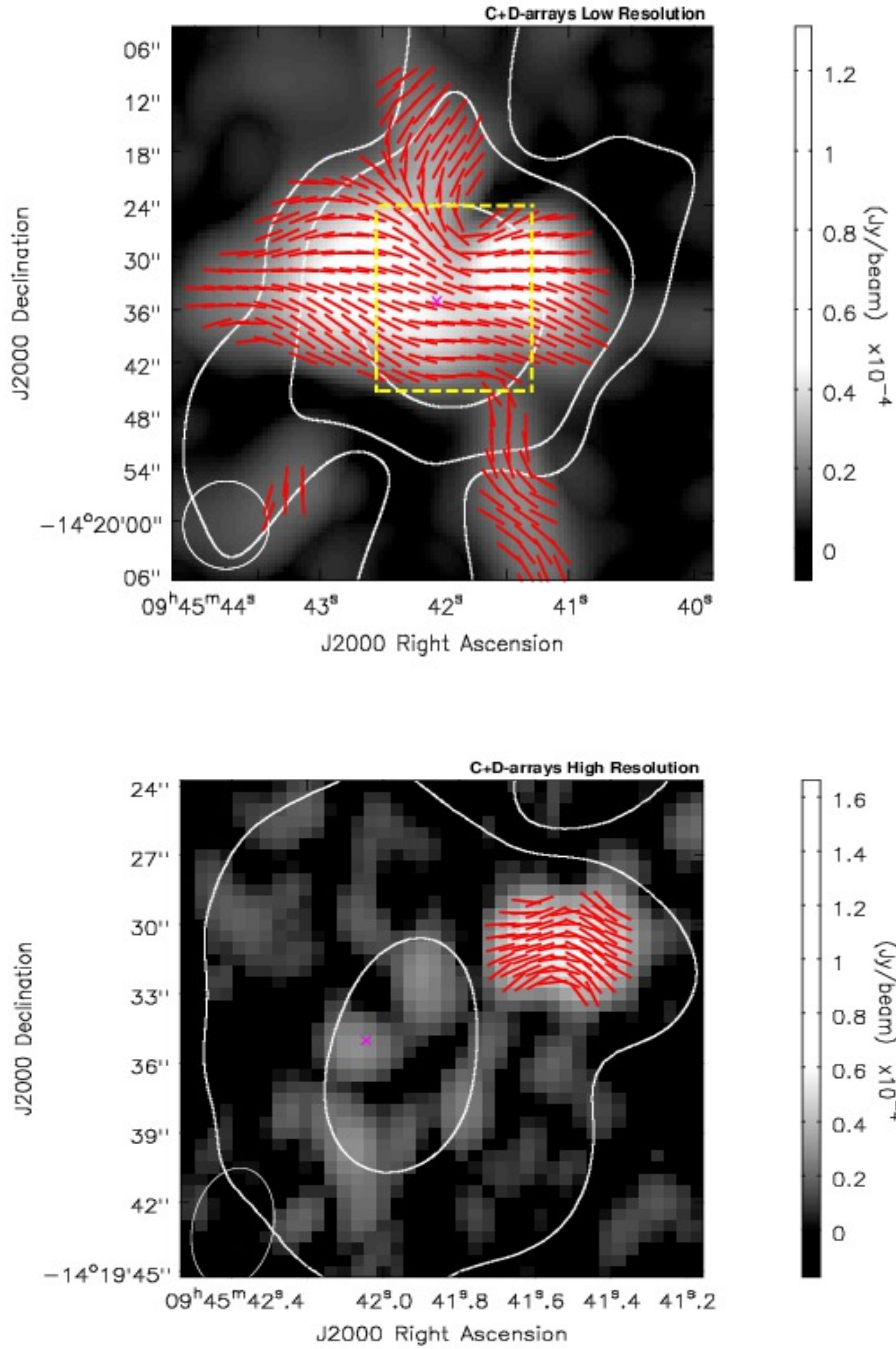


Fig. 4.— Combined C-band C+D configuration polarization images (greyscale) with matching configuration and resolution total intensity contours (white) and B vectors (red, *Faraday corrected*). The NED center is marked with an X. **Top:** Low resolution 10 x 10 arcsec image. Contours are 75 ( $5\sigma$ ), 200, and 4000  $\mu\text{Jy beam}^{-1}$ . The peak polarized intensity is 69.1  $\mu\text{Jy beam}^{-1}$  (in the west peak). The yellow dashed box shows the approximate field of view of the bottom image. **Bottom:** High resolution 5 x 3 arcsec image. Contours are 25 ( $5\sigma$ ), 200 and 10000  $\mu\text{Jy beam}^{-1}$ . The maximum polarized intensity is 60.2  $\mu\text{Jy beam}^{-1}$ .

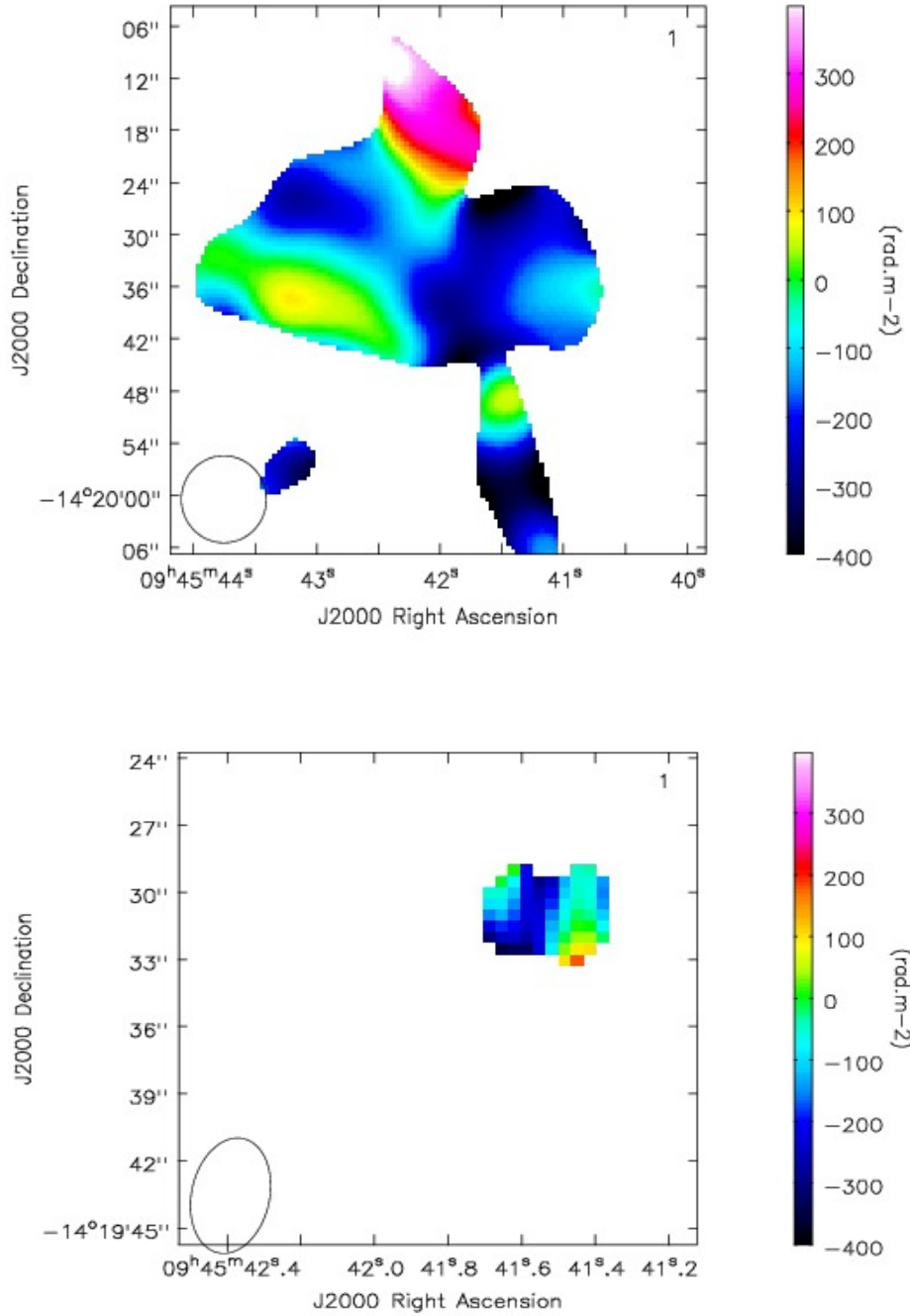


Fig. 5.— Combined C-band C+D configuration RM images that correspond to Fig. 4 with the low resolution image at top and high resolution image at bottom. The corresponding beams are shown at lower left.

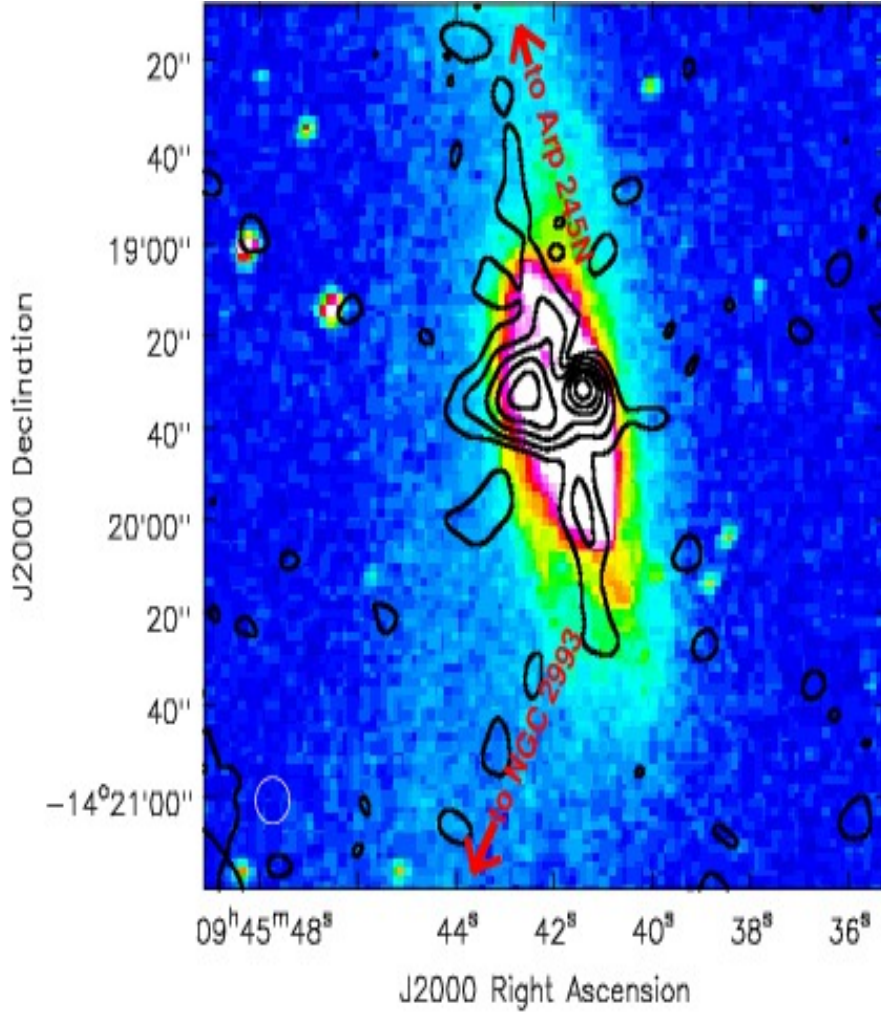


Fig. 6.— Combined C-band C+D configuration low resolution polarization images (contours, PB-corrected) superimposed on an optical DSS2 blue image. Contours are 10.5 ( $3\sigma$ ), 20, 30, 40, 50, and 62  $\mu\text{Jy beam}^{-1}$ . The directions towards the companion galaxies are marked and the synthesized beam is shown at lower left.



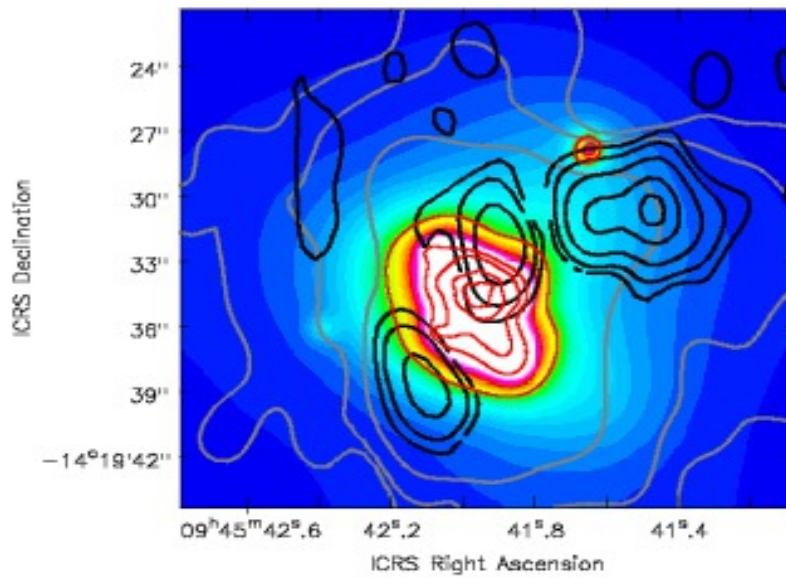


Fig. 7.— CHANDRA X-ray image of NGC 2992 in the 0.5 - 4 keV range (colour) which has been adaptively smoothed with the CIAO routine *csmooth* with a Gaussian kernel whose size is locally adjusted to achieve a signal-to-noise ratio between 2 - 2.5. Grey contours are the lowest 3 contours of the C-configuration total intensity image as shown in Fig. 1, and black contours are the same contours as shown in the polarized intensity image as shown in Fig. 3 (top). Four high level X-ray contours are shown in red.

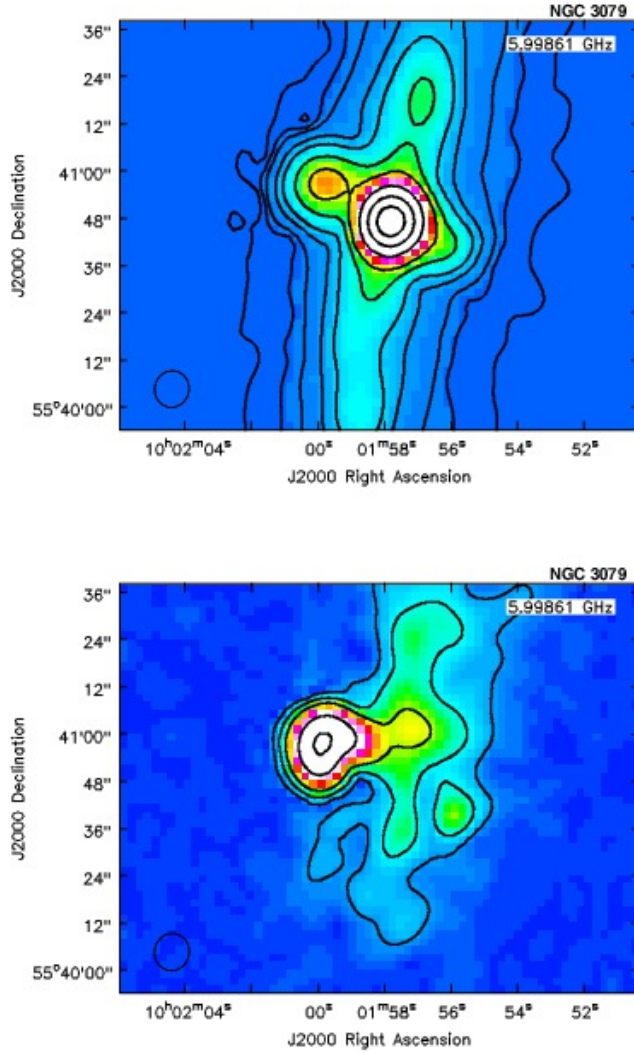


Fig. 8.— **Top:** D-configuration C-band total intensity map of NGC 3079 (colours and contours). The contours are at 10, 25, 50, 150, 300, 700, 1300, 4000, 10000, and 20000 times the rms noise of  $6.5 \mu\text{Jy beam}^{-1}$ . **Bottom:** D-configuration C-band linear polarization map of NGC 3079 (colours and contours). The contours are at 10, 25, 50, 150, and 300 times the rms noise of  $5.9 \mu\text{Jy beam}^{-1}$ . Both maps are adapted from Wiegert et al. (2015) and the beams, of dimensions 9.3 by 8.7 arcsec at a position angle of  $-13.9$  deg., are shown at lower left.